RSC Advances

PAPER

View Article Online
View Journal | View Issue

Cite this: *RSC Adv.*, 2025, **15**, 30394

Mineralogical characterization and fluorescence properties of blue, yellow and green apatite

Wenkai Liang, Nai Wang * and Yingrui Gan

Blue, yellow and green are common colors of apatite, and its mineralogical characteristics and fluorescence properties have attracted the attention of many researchers and scholars. In this paper, the structure, composition, spectroscopic features and fluorescence characteristics of three different colors of apatite are investigated to further compare and explore their mineralogical characteristics and fluorescence properties. The results show that the three colors of apatite that belong to fluorapatite, blue apatite and green apatite are in medium oxidation state, and yellow apatite is in oxidation state. Some samples of blue and green apatite showed the homogeneous substitution of $[CO_3]^{2-}$ for $[PO_4]^{3-}$. Yellow apatite fluoresces orange, green and blue apatite fluoresce blue–violet, and all three colors of apatite show strong emission peaks at 400 nm at an excitation wavelength of 320 nm, attributed to: the jump of Ce^{3+}: $(5d)^5D_{3/2} \rightarrow {}^2F_{7/2}(4f)$ to $(5d)^5D_{3/2} \rightarrow {}^2F_{5/2}(4f)$, and the jump of Eu^{2+}: $4f^65d^1 \rightarrow (4f)^8S_{7/2}$; The emission peaks at 585 nm and 600 nm are attributed to the leaps of ${}^4G_{5/2} \rightarrow {}^6H_{7/2}$ for Sm^{3+} with ${}^1D_2 \rightarrow {}^3H_4$ for Pr^{3+}. A comparative analysis of the relationship between luminescence intensity and temperature in samples of yellow and blue apatite was conducted. The findings of this analysis indicated that yellow apatite exhibits greater thermal stability in comparison to blue apatite.

Received 11th May 2025
Accepted 18th August 2025

DOI: 10.1039/d5ra03299g

rsc.li/rsc-advances

1 Introduction

Apatite is a calcium-bearing phosphate mineral that is found in a variety of geological settings and rock formations. The general formula of its crystal structure is $A_5(XO_4)_3(Z)$, and the A-site Ca^{2+} can be substituted by other divalent cations, rare-earth element ions, and alkali metal ions in an isomorphism; XO_4^{4-} represents the anionic complexes which can be: AsO_4^{3-}, SO_4^{2-}, CO_3^{2-}, and SiO_4^{4-}, and the Z-site is predominantly occupied by F, OH, and Cl ions, and apatite is classified as fluorapatite, hydroxyapatite, and chlorapatite based on the Z ions.[1–4] Natural apatite is a popular substance among consumers due to its vibrant colors and diverse luminescent properties. Under UV fluorescent irradiation, this mineral emits a spectrum of colors, including blue, purple-pink, and green.

In the field of mineralogy, apatite is a prevalent by-mineral in a variety of igneous, metamorphic, and sedimentary rocks. Its structural and compositional characteristics yield substantial insights into petrogenesis and mineralization processes. Extensive research has been conducted on various aspects, including dating methods, low-temperature pyroclastic studies, isotope tracing, and deposit geochemistry.[5] Apatite is characterized by its abundance of primary and trace elements, with its original information being more effectively preserved post-formation. For instance, the SO_3 composition of apatite can be used to estimate the sulfur content in the magma of the ore-forming host rock. The halogen content can be used to estimate the F, Cl, and H_2O content in the fluids and melts, and trace elements (Mn, Ce, Eu, *etc.*) can indicate the redox state of the ore-forming rocks. Finally, Sr-Nd isotopes can trace the origin and evolution of the ore-forming magma or hydrothermal fluids.[6] Apatite has long been recognized as a crucial instrument in the field of mineralogical research.

Due to its multiple lattice sites and variable crystal field environment, apatite has been widely studied in the field of mineral luminescence and is considered a perfect fluorescence mechanism.[7] The fluorescent properties of apatite are widely used, and apatite-structured compounds are practical matrices,[8,9] and numerous apatite-type luminescent materials have been prepared by some researchers and scholars in the past few years.[10–12] Fluorapatite is the most luminescent subspecies within the apatite mineral group, and its dual luminescence mechanism, involving phosphorescence and fluorescence, its capacity for rare earth elements to regulate, and its stable crystal structure, all render it indispensable in the domains of gem identification and luminescent materials research. There is a wealth of research information on the luminescent properties of natural and synthetic apatite phosphors, and the research techniques are mainly laser-induced photoluminescence spectroscopy,[13,14] and Laser-induced

School of Gemmology, China University of Geosciences, Beijing, 100083, China. E-mail: 2003011807@cugb.edu.cn

delayed luminescence (LIDL). Reisfeld *et al.* detected the luminescent centers of Pr^{3+}, Eu^{3+}, Er^{3+}, Tm^{3+} and Yb^{3+} in apatite using laser-induced luminescence;[13] Gaft *et al.* utilized laser-induced luminescence to detect the long-decay luminescence center of Eu^{3+} and to identify high symmetry position of Ca(1) in the Eu^{3+}- substituted apatite.[15] This was soon followed by the detection of the Pr^{3+} luminescence center using the aforementioned technique. It was ascertained that the different spectral properties of Pr^{3+} were related to its structural position of Ca within the apatite;[16] A group of scholars conducted a study in which they examined the apatite of varying rock types utilizing steady-state fluorescence spectroscopy. They further characterized the luminescence characteristics of Ce^{3+} and Eu^{2+} in apatite. Their findings revealed that Ce in apatite attains two distinct wavelength ranges at two distinct Ca crystalline locations: 340 to 380 nanometers (nm) for Ca(I) and 420 to 450 nm for Ca(II);[17] M. Czaja *et al.* detected luminescence spectra in apatite attributable to Sm^{3+}, Pr^{3+}, and Eu^{3+}, in addition to the presence of Ce^{3+} and Eu^{2+} ions, as detected by selective excitation of steady-state fluorescence.[18] The fluorescence behavior of different color apatite varies significantly. Specifically, blue–violet fluorescence is mostly triggered by Ce^{3+}, Dy^{3+}, and Eu^{2+}, while orange–red fluorescence is associated with Pr^{3+} and Sm^{3+}[19]. The underlying mechanisms behind the fluorescence phenomena exhibited by different colored apatite remain to be fully elucidated. Therefore, a comparative analysis of the fluorescence properties across diverse apatite colors is imperative to comprehensively understand their respective fluorescence characteristics.

Consequently, natural apatite samples in blue, yellow, and green colors were selected in this paper, and their chemical compositions, crystal structures, spectral characteristics, and fluorescence properties were discussed comprehensively. This study innovatively utilizes fluorescence spectroscopy and variable temperature fluorescence spectroscopy to analyze apatite. The aim is to explore the fluorescence characteristics of three colors of apatite and the effect of temperature on the fluorescence changes, and to broaden the potential applications of apatite in the field of luminescence.

2 Materials and methods

2.1. Materials

Blue, yellow, and green apatite samples were selected and purchased from network suppliers of raw stones. The blue apatite was numbered APB-1 to APB-5; the yellow apatite was numbered APY-1 to APY-5; and the green apatite was numbered APG-1 to APG-5. The samples were all raw stone as shown in Fig. 1.

2.2. Methods

X-ray powder diffraction (XRD) tests were conducted using the Bruker D8Advance diffractometer at the School of Materials Sciences and Technology, China Uinversity of Geosciences, Beijing. Equipped with Cu Kα radiation ($\lambda = 1.5406$ Å) running at 40 kV and 30 mA.

The composition of apatite was tested using an EPMA-1720 electron microprobe from Shimadzu, Japan, with a detection limit of 500 ppm. Voltage set to 15 kV, carbon coated before testing.

Trace element testing was performed using an Analytik Jena Plasma Quant MS, (Jena, Germany) laser-ablation inductively coupled plasma mass spectrometer (LA-ICP-MS). The laser stripping system was a quasi-molecular laser with a resolution of 193 nm, and high-purity helium was used as the carrier gas for the experiment. The single-point analysis time was 85 s, of which the blank background acquisition time was 20 s, the continuous stripping acquisition time was 45 s, the cleaning of the injection system time was 40 s, and the sample acquisition data point size was 100 μm.

Infrared spectroscopy, Raman spectroscopy and UV-visible absorption spectroscopy were carried out at the Gem Testing Laboratory, the School of Gemology, China University of Geosciences (Beijing). Infrared spectroscopic data were acquired utilizing a TENSOR 27 Fourier transform infrared spectrometer manufactured in Germany. The measurements were conducted in reflectance method with a spectral scanning range spanning from 200 cm^{-1} to 4000 cm^{-1} Raman spectra were acquired using an HR Evolution micro-Raman spectrometer (HORIBA, Japan). The experimental voltage was 220 V, the current was 10

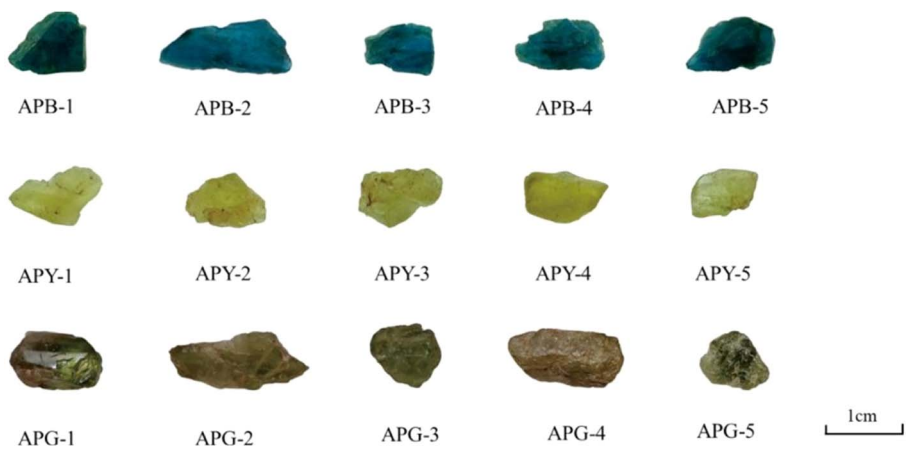

Fig. 1 Picture of apatite samples.

A, the laser wavelength was 532 nm, and the scanning range was 100–4000 cm^{-1}. UV-vis absorption spectra were recorded using a UV-3600 UV-vis spectrophotometer (Shimadzu, Japan). The experimental conditions were as follows: the sampling interval was 2 s; the testing method was diffuse reflection method; the measuring wavelength range was 200–900 nm.

A Hitachi F-4700 fluorescence spectrophotometer equipped with a temperature control unit was used to obtain photoluminescence spectra, photoluminescence excitation spectra, and variable-temperature photoluminescence spectra of the samples. The scanning rate was 1200 nm min^{-1}, the detection voltage was 500 V, and the warming rate of variable-temperature fluorescence was 0.17 K s^{-1}, with a warming range of 300–575 K. The temperature range of the fluorescence was from 300 to 575 K, and the temperature range of the fluorescence was 0.17 K s^{-1}.

3 Results and explorations

3.1. XRD tests of apatite

As shown in Fig. 2, the XRD patterns of blue, yellow and green apatite are in general agreement with that of the standard card PDF#15-0876, and all diffraction peaks reflect the phase of apatite $Ca_5(PO_4)_3F$ well, suggesting that there is no structural difference between apatite samples of different colors. Apatite has a high degree of crystallinity as indicated by the sharp shape of the XRD peaks of the samples. The strongest diffraction peak of apatite is 31.803° in 2-Theta, followed by 32.953°, 28.97°, 32.183°, 39.86° and 49.472°. The blue apatite APB-3 has a space group of $P6_3/m$ with cell parameters $a_0 = b_0 = 9.405$ Å, $C_0 = 6.8751$ Å, $\alpha = \beta = 90°$, $\gamma = 120°$. Green apatite APG-2 has a space group of $P6_3/m$, $a_0 = b_0 = 9.4010$ Å, $C_0 = 6.9843$ Å, $\alpha = \beta = 90°$, $\gamma = 120°$. The space group of yellow apatite APY-4 is $P6_3/m$ with cell parameters $a_0 = b_0 = 9.4553$ Å, $C_0 = 7.0195$ Å, $\alpha = \beta = 90°$, $\gamma = 120°$. In apatite there is a significant decrease in the cell parameter a with an increase in the structural carbonate content, while c remains essentially constant. However, substitution between channel ions (F^-, OH^-, Cl^-) is the main factor influencing the cell parameters in most magmatic apatite.[20–22] By fitting the calculated cell parameters of different colored apatite, it can be observed that the blue and green series apatite, which show carbonate ion isomorphism substitution, have reduced a values compared to the yellow series apatite, which do not show substitution, and the carbonate content should be higher in the blue apatite than in the green apatite. It indicates that the apatite samples are all fluorapatite and that the isomorphism substitution phenomenon is less influential.

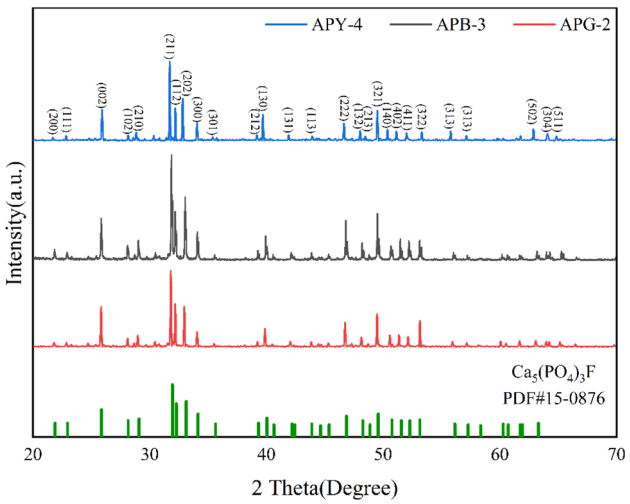

Fig. 2 XRD data for three colors of apatite.

3.2. Analysis of chemical composition

3.2.1. Electronic probe tests. Chemical composition analysis is an essential method for mineral analysis, and Electron probe microanalysis (EPMA) can accurately analyze the chemical composition at specific points. The EPMA results are shown in Table 1. The main components of apatite are CaO and P_2O_5, and the contents of the two components show a similar trend. The three colors of apatite samples do not differ much in the contents of CaO and P_2O_5, and all of them show F^- rich and Cl^- poor characteristics, with the contents of F in the range of 2.16–3.67 wt% and Cl in the range of 0.14–1.30 wt%, and the F/Cl The range of the average values was 1.67–26.79. Second, the content of Ce_2O_3 is highly variable, green series > yellow series > blue series. The contents of FeO, MnO, and As_2O_3 are almost all very small, with FeO contents ranging from 0 to 0.09 wt%, MnO contents ranging from 0 to 0.13 wt%, all less than 0.1 wt%; and As_2O_3 contents ranging from 0 to 0.06 wt%. The Mn and Fe content of this test was not very high, with Mn/Fe ranging from 0 to 10.13, and H.B. Ribeiro *et al.* found that when the Mn/Fe in apatite is less than 1, it inhibits the luminescence of apatite.[23] In this study there were fewer samples with Mn/Fe less than 1. All three colors showed fluorescence inertness or relatively weak fluorescence under UV fluorescent lamps, presumably due to contamination of the sample surfaces or the use of fluorescent lamps with low energy during testing.

Three of each color sample were selected for calculation of their crystal chemical formulas by the oxygen atom method. In the blue, yellow and green series apatite, Ca^{2+} was partially replaced by ions such as Na^+, Ce^{3+}, Sr^{2+}, Fe^{2+}/Fe^{3+} and Mn^{2+} were observed, whereas $[PO_4]^{3-}$ anionic groups were replaced by $[SiO_4]^{4-}$, and $[SO_4]^{2-}$ isomorphic substitution occurred more frequently in apatite, indicating that the crystal structure has a certain degree of flexibility that can be replaced by a variety of cations and anions. By calculation, it can be found that the content of F^- in the general formula of apatite of the three colors is greater than the content of Cl^- and OH^-, so the additional anions of the end elements are dominated by F^-, and it can be determined that all the apatite samples in this test are fluorapatite.

3.2.2. LA-ICP-MS test. LA-ICP-MS tests were performed to investigate the trace element composition of three colors of apatite. The results calculated using spherulitic meteorite data (Sun & McDonough, 1989) were used. Rare earth element (REE) data from the present LA-ICP-MS measurements were used to prepare REE partitioning maps for three different colored

Table 1 Some Electron probe microanalysis (EPMA) results for different colored apatite (in wt%)

Date	APY-5	APY-3	APY-1	APG-5	APG-4	APG-2	APB-5	APB-3	APB-1
CaO	52.94	52.09	51.80	54.40	52.48	52.88	54.00	54.13	54.52
P_2O_5	41.05	40.57	40.43	40.13	40.45	39.96	40.41	40.22	40.25
SO_3	0.20	0.42	0.42	0.98	0.85	0.99	0.90	0.70	0.56
SiO_2	0.20	0.43	0.42	1.02	0.89	1.13	1.21	1.04	1.18
Na_2O	0.20	0.21	0.26	0.18	0.06	0.17	0.01	0.00	0.00
MgO	0.12	0.11	0.04	0.00	0.00	0.00	0.00	0.00	0.01
Al_2O_3	0.01	0.00	0.00	0.00	0.00	0.02	0.01	0.02	0.02
FeO	0.06	0.12	0.06	0.00	0.00	0.00	0.00	0.03	0.00
MnO	0.13	0.08	0.09	0.00	0.00	0.00	0.03	0.03	0.10
SrO	0.24	0.21	0.17	0.35	0.34	0.24	0.05	0.04	0.13
La_2O_3	0.30	0.30	0.31	0.37	0.21	0.37	0.10	0.13	0.21
TiO_2	0.00	0.01	0.03	0.03	0.00	0.00	0.00	0.06	0.02
Ce_2O_3	0.87	0.74	0.89	0.65	0.71	0.82	0.22	0.35	0.45
Nd_2O_3	0.27	0.21	0.32	0.21	0.21	0.23	0.16	0.01	0.14
As_2O_3	0.00	0.01	0.00	0.01	0.00	0.00	0.06	0.00	0.00
F	2.16	2.72	2.41	3.37	3.71	2.24	3.29	3.30	3.67
Cl	1.30	1.22	1.21	0.32	0.20	0.34	0.19	0.16	0.14
Ca/P	1.63	1.63	1.62	1.72	1.64	1.68	1.69	1.71	1.72
Mn/Fe	2.47	0.65	1.55	0.00	0.00	0.00	0.00	0.98	0.00
F/Cl	1.67	2.23	2.00	10.54	18.82	6.61	17.42	20.89	26.79
Total	100.05	99.44	98.83	102.01	100.11	99.37	100.64	100.22	101.39

apatite samples following the spheroidal meteorite standardization method. Detailed data are provided in SI S-1 and S-2.

As Fig. 3 and Table 2 show, the three colors of apatite exhibit a consistent "rightward shift" in the distribution of rare earth elements. This trend is characterized by an enrichment of light rare earth elements and a deficiency of heavy rare earth elements. It should also be noted that the elements Eu and Ce are present. Through the formula $\delta Eu = \frac{2Eu_N}{Sm_N + Gd_N}$; $\delta Ce = \frac{2Ce_N}{La_N + Pr_N}$, where a positive anomaly is defined as $\delta > 1$ and a negative anomaly as $\delta < 1$, it can be determined that the blue apatite sample has a δEu value of 0.43 and a δCe value of 0.84, indicating a negative Eu anomaly. Additionally, Ce exhibits a negative anomaly, though it is not pronounced; The green apatite sample has a δEu of 0.40 and a δCe of 0.84, exhibiting a negative Eu anomaly, while Ce also shows a negative anomaly but it is not significant; The yellow apatite sample has a δEu of 0.66 and a δCe of 0.85, exhibiting a moderate negative Eu anomaly, while Ce shows a negative anomaly but it is not significant. The magmatic evolution process is accompanied by changes in oxygen fugacity, and in apatite Eu and Ce are two widely differing elements with opposite distribution characteristics, so this property is an important indication for identifying the oxidation state of apatite.[24,25] Under the same conditions of temperature, pressure, and magma composition, apatite crystals from highly oxidized magmas have higher levels of Eu, V, and As and lower levels of Mn, Ce, and Ga compared to apatite crystals from less oxidized magmas.[25] However, the redox state of apatite cannot be determined by the valence and content of a single element because feldspathic deviation results in a lower level of Eu. Therefore, conclusions regarding the redox state of this apatite sample must be drawn in conjunction with further research.

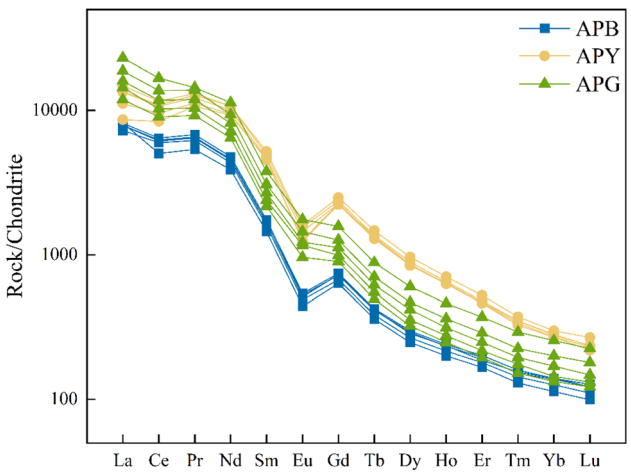

Fig. 3 Standardized elemental assignments for three colors of apatite globular meteorites.

3.3. Spectroscopy analysis of apatite

3.3.1. Infrared spectra analysis. Apatite samples were tested using the reflectance method to compare the infrared spectral characteristics of different colors. The transmission method was used as a complementary experiment for possible missing OH^- data. The test results are shown in Fig. 4. Comparing the infrared spectra of apatite of three colors, it can be seen that the sample apatite has the following infrared spectral features in the range of 400–1800 cm^{-1}: the absorption peaks near 574 cm^{-1}, 590 cm^{-1} and 605 cm^{-1} are the bending vibrational peaks V_4 of $[PO_4]^{3-}$; the weak absorption peaks at 960 cm^{-1} are the symmetric telescoping vibrational peaks V_1 of $[PO_4]^{3-}$; the absorption peaks near 1045 cm^{-1} and 1101 cm^{-1}

Table 2 Rare earth elements content of three colors of apatite

Samples	APB1-5	APG1-5	APY1-5
Total rare earth elements (ΣREE) range (μg g^{-1})	7852.12–9361.13	12978.76–23730.23	14197.93–18619.40
Light rare earth elements (LREE) mean (μg g^{-1})	8447.77	17127.90	15817.89
Heavy rare earth elements (HREE) mean (μg g^{-1})	301.86	477.27	930.25
δEu	0.43	0.40	0.66
δCe	0.84	0.84	0.85

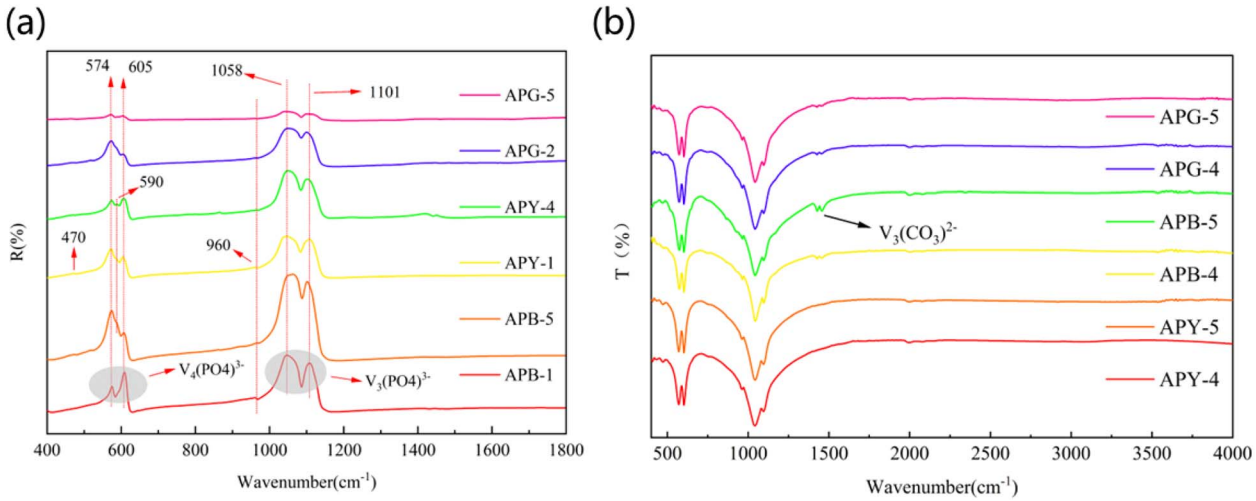

Fig. 4 Infrared spectra of three colors of apatite (a) reflectance method (b) transmission method.

are the asymmetric telescoping vibrational peaks V_3 split by $[PO_4]^{3-}$; the absorption peaks near 1045 cm^{-1} and 1101 cm^{-1} are split by the asymmetric stretching vibrational peak V_3 of $[PO_4]^{3-}$. There is also a weak absorption peak at 470 cm^{-1} in the yellow series apatite, caused by the V_3–V_4 differential frequency mode. In the green series of apatite, the symmetric telescopic vibrational peak V_1 at 960 cm^{-1} by $[PO_4]^{3-}$did not appear except for APG-2, and the intensity of the individual absorption peaks of APG-5 was lower than that of the other samples. Gillespie J *et al.* concluded that the IR reflectance spectra in apatite are related to the P content of the sample, and the higher the P content the higher the intensity of the associated vibrational peaks.[26] In the IR transmission spectra, as shown in Fig. 4b, none of the apatite samples showed a vibrational peak at 3570 cm^{-1}. It is assumed that the present apatite samples are all fluorapatite. The blue series of apatite samples showed significant absorption peaks at 864 cm^{-1}, 1432 cm^{-1} and 1456 cm^{-1} in the infrared transmission spectrum; the green series of apatite samples showed weak absorption twin peaks at 1435 cm^{-1} and 1459 cm^{-1}, and the vibration twin peaks of $[CO_3]^{2-}$ in the yellow series of samples were not evident. The infrared spectrum of $[CO_3]^{2-}$substitution of $[PO_4]^{3-}$ shows the absorption peak positions of $[CO_3]^{2-}$, generally located at 870 cm^{-1}, 1420 cm^{-1}, and 1450 cm^{-1}, the former being the V_2 vibration of $[CO_3]^{2-}$, and the latter two being attributed to the V_3 vibration and splitting, and thus it is hypothesized that the appearance of the $[CO_3]^{2-}$substitution of $[PO_4]^{3-}$ occurs in blue and green colors apatite samples.[27,28]

From the IR transmission and reflection results, in addition to the weak $[CO_3]^{2-}$ characteristic peaks observed in the blue and green apatite samples, it is clear that the characteristic peaks appearing in the vibrational spectra of the three colored apatite samples are mainly caused by the vibrations of the phosphorus–oxygen tetrahedra. The vibration of infrared reflection and transmission spectra of different color apatite has no significant change, only in the intensity of the peaks have been affected by the polarization rate and elemental content.

3.3.2. Raman spectra analysis. In the context of Raman spectroscopy, the vibrational peaks of anionic groups are predominantly distributed within the wavelength range of 400 to 1500 cm^{-1}, while the vibrational peaks of the additional anion $[OH]^{-}$ are primarily situated at approximately 3500 cm^{-1}. Consequently, two segments of the wavelength ranges of 400 to 2200 cm^{-1} and 3200 to 3600 cm^{-1} were selected for the present study to facilitate exploration. Laser Raman experiments have been carried out on samples of apatite in three different colors, and the results of the experiments are shown in Fig. 5. The Raman spectra of the blue and green samples are approximately the same, and the yellow sample has fewer spurious peaks, indicating that its sample composition is more homogeneous. The spectrum appears to be shifted upward from left to right because the Raman laser-irradiated portion is excited with fluorescence, causing the spectrum to appear shifted.

There were four distinct absorption peaks in the range of 400 to 2200 cm^{-1} and one distinct absorption peak in the range of

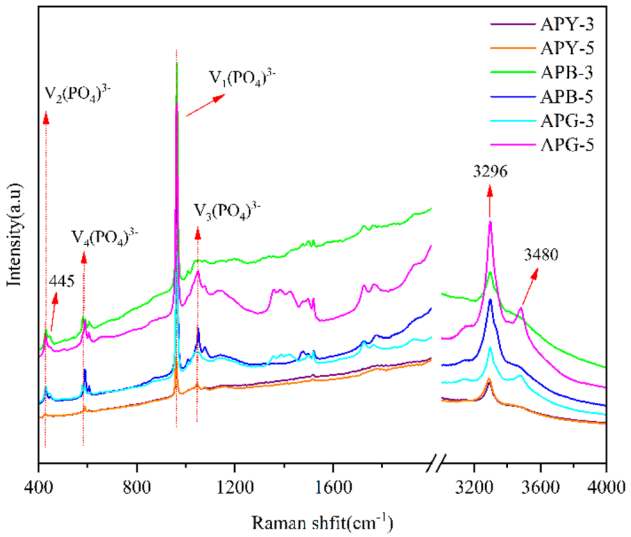

Fig. 5 Raman spectra of three color apatite.

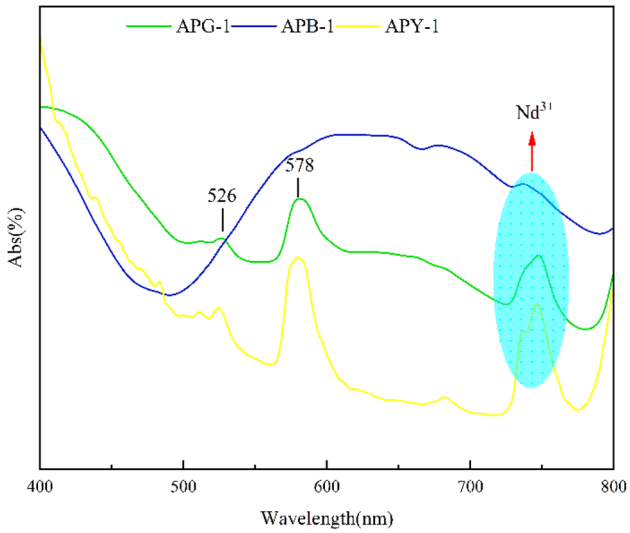

Fig. 6 UV-visible spectra of three different colors of apatite.

3200 to 3600 cm^{-1}. Comparing the laser Raman spectra of the three colors of apatite, the vibrational peaks of phosphate were mainly appeared, and the symmetric vibration of V_1 of $[PO_4]^{3-}$ showed the strongest vibrational peak at 959–962 cm^{-1}; the bending vibrational peak of V_2 was weaker and was located in the range of 430–450 cm^{-1}; the asymmetric telescopic vibrational absorption peak, V_3, showed the weak vibration at the location of 1050 cm^{-1}; and the V_4 asymmetric bending vibration peak, with weak vibration at the range of 577∼603 cm^{-1}. In the range of 3200–3600 cm^{-1}, the samples all showed absorption peaks at 3480 cm^{-1}, which was caused by the O–H stretching vibration, and also showed a weak absorption peak at 3296 cm^{-1}. The vibrational mode of $[CO_3]^{2-}$ in the Raman spectrum is a symmetric vibration at 1070 cm^{-1}, and the other vibrational peaks of $[CO_3]^{2-}$ in the Raman spectrum are not obvious due to the asymmetric telescopic vibration V_3 of $[PO_4]^{3-}$ is located at 1050 cm^{-1}, which is easy to overlap. In combination with the infrared transmission spectra of the samples and the XRD analysis of the composition, it is hypothesized that the blue and green apatite samples show a substitution of $[CO_3]^{2-}$for $[PO_4]^{3-}$. In addition, a weak absorption peak at 3296 cm^{-1} was detected. This peak is probably caused by water in apatite.[29]

3.3.3. UV-vis spectra. Blues, greens, and yellows are common in apatite, and the color of apatite is often a transition between these three colors. UV testing of three colors of apatite samples, the results Fig. 6 shows that yellow and green apatite samples UV spectra are similar, the presence of absorption peaks near 526, 579, 737, 748, blue apatite in the blue zone appears transmittance region, 580–725 nm of the yellow zone to the red zone appears a significant intensity of the broad absorption band, 737 nm there is a tiny absorption peak. From previous studies, 526, 579, 737, and 748 are known to be caused by electronic orbital jumps of rare earth Nd^{3+} corresponding to the energy levels of Nd^{3+} assigned to $^4G_{7/2}$, $^2G_{7/2}$, $^4S_{3/2}$, and $^4F_{7/2}$, respectively.[14,30] It is presumed that the color of yellow series and green series apatite is related to Nd^{3+}; The broad absorption band of 580–725 nm in blue series apatite may be related to MnO_3^- and SO_3^-,[23,31] as the original absorption peaks in the crystals tend to show widening phenomenon due to the rare earth ions, and the trace amount of Mn and Fe can have an effect on the color, and the Mn/Fe ratio has a significant effect on the UV-visible absorption,[32] the absorption is mainly concentrated in the yellow, red and violet regions.

Comparing the UV-visible spectra of the three colors of apatite, the three colors of apatite absorb strongly in the blue-violet region, and the absorption of the yellow and green series samples is larger than that of the blue series samples, and the absorption in the blue-violet range is mainly related to Ce.[33] In the yellow series apatite, there is no absorption band of 600–750 nm, and there is an absorption peak belonging to Nd^{3+}, so the coloring mechanism of yellow apatite is mainly related to Nd^{3+}. Green apatite, there is an absorption band of 600–750 nm, and the absorption peak belongs to Nd^{3+}, which is the reason why the green series apatite has a yellow hue. The coloring mechanism of blue apatite is mainly related to MnO_3^- and SO_3^-.Comparing the Nd content, the Nd content of APY-1 > Nd content of APG-1 > Nd content of APB-1 is presumed to be related to the wavelength redshift of the sample colors, because the absorption peaks induced by Nd^{3+} were observed in all the three colors of apatite, and there was a deviation in the position of the absorption peaks. The absorption bands at 610–720 nm of each color of apatite have different contributions, and the absorption band of APY-1 is weak, which is caused by the influence of transition metals Mn and Fe, while the absorption bands of APG-1 and APB-1 have not only the contribution of transition metals, but also the contribution of Th element, which can be used as a marker for the presence of SO_3^- and SiO_3^- radicals, and the content of Th in the blue series of apatite is much higher than that of the remaining two colors. Th content of blue series apatite is much higher than that of the other two colors.

3.4. Analysis of apatite fluorescence properties

3.4.1. Steady-state fluorescence performance. The emission spectra of apatite samples collected under excitation sources of 254 nm and 365 nm are shown in Fig. 7. Results show that the samples fluoresce weakly at 365 nm, with low emission intensity and similar emission peaks. The emission peak at 397 nm found in the sample of APY with APG in the emission spectrogram of $\lambda_{ex} = 254$ nm.

The fluorescence spectra of the three colored apatite samples show that the blue and green samples have similar fluorescence spectra, while the yellow sample has a different luminescence behavior, as shown in Fig. 8a. Fluorescence emission peaks were found at 400 nm for all three colors samples and also at 585 and 600 nm for the yellow series. As shown in Fig. 8b, a Gaussian fit was performed on the 400 nm fluorescence emission peak. Three small peaks at 393 nm, 409 nm and 434 nm were fitted to the emission peak. The emission peaks at 400 nm can be attributed to the leaps of Ce^{3+}: $(5d)^5D_{3/2} \rightarrow {}^2F_{5/2}(4f)$ as well as $(5d)^5D_{3/2} \rightarrow {}^2F_{5/2}(4f)$ and Eu^{2+}: $4f^65d^1 \rightarrow (4f)^8S_{7/2}$, which are a combined effect of the jumps of the two rare earth ions.[34,35] LA-ICP-MS test results showed that the Eu content in apatite samples ranged from 31.34 to 101.88 ppm. Previous studies have shown that strong blue-violet fluorescence can be produced at a wavelength[36] of 266 nm when the Eu content is 20 $\times 10^{-6}$, and that Ce^{3+} can act as a sensitizer for other rare earth ions.[19] The two elements work together to produce fluorescence. The emission peaks of the green and blue samples showed different degrees of redshift at 400 nm with respect to the emission peaks of the yellow samples, and the phenomenon of peak shift was generally investigated by the previous researchers using the crystal field intensity analysis method[37] according to the crystal field intensity calculation formula:

$$D_q = \frac{1}{6} Ze^2 \frac{r}{R^5}$$

Among these, D_q refers to energy level splitting; z is the charge of the anion ligand; e is the electron charge; r is the radius of the d wave function; and R is the bond length. In apatite samples, since the values of d, z, e, and r are identical, the energy level splitting (D_q) is inversely proportional to R. According to the results of Electron probe microanalysis (EPMA) data test, all three color samples contain Na and Mg ions, so there will be the phenomenon of Na, Mg into the Ca site, the degree of substitution: yellow series > green series > blue series, because the ionic radius of Na, Mg is smaller than the ionic radius of Ca, so Na, Mg ions into the crystal lattice to replace ions larger than their own ionic radius. Based on the above equations, the entry of sodium and magnesium ions into the crystal lattice causes R to decrease, the crystal field splitting energy to increase, and the emission peak to exhibit a red shift phenomenon. However, as shown in Fig. 8, the actual situation is exactly the opposite. Therefore, for naturally occurring apatite minerals with more complex compositions, calculations of crystal field strength contribute little to explaining changes in peak positions. It is therefore speculated that the red shift observed in the fluorescence spectra of the three colored apatite samples is due to the different lattice positions of the luminescent centers Ce and Eu at an excitation wavelength of 320 nm, resulting in a red shift of the 400 nm emission peak.

The emission peaks at 585 nm and 600 nm are attributed to the leaps of Sm^{3+} and Pr^{3+}, respectively, in the mode of ${}^4G_{5/2} \rightarrow {}^5H_{7/2}$ for Sm^{3+} and ${}^1D_2 \rightarrow {}^3H_4$ for Pr^{3+}. Pr^{3+} displaces the Ca(I) position in natural fluorapatite and produces a brick-red fluorescence around 610 nm.[18,38] In fluorescence phenomena, Pr^{3+} sensitizes other rare earth elements more than it sensitizes its own emission, if Pr^{3+} and Sm^{3+} have similar characteristic jump energies.[38,39] The emission intensity is strong for the yellow sample, weak for the green sample, and no corresponding emission peaks are observed for the blue sample. Comparing the Sm content of the three colored apatite samples, the average Sm content in the yellow sample was 730.76 ppm, the average Sm contant in the green sample was 431.42 ppm, and the average Sm content in the blue sample was 248.87 ppm, and the yellow sseries had the highest Sm content, so the yellow apatite showed a stronger emission peak at 585 nm, and Sm^{3+} had a Pr^{3+} sensitizing effect. When Sm and Pr ions are in close

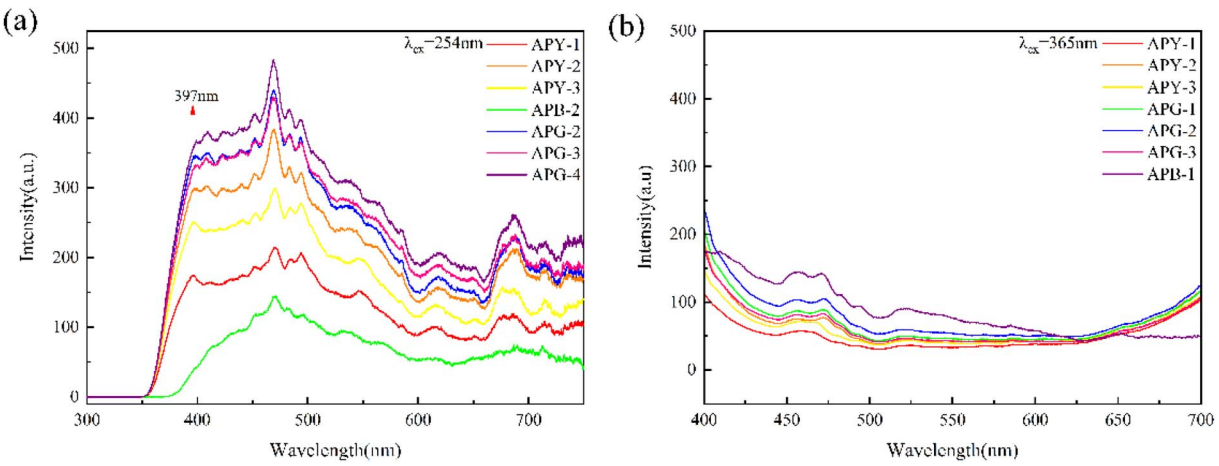

Fig. 7 (a) Emission spectra of different colored apatite samples at an excitation wavelength of 254 nm; (b) emission spectra of different colored apatite samples at an excitation wavelength of 365 nm.

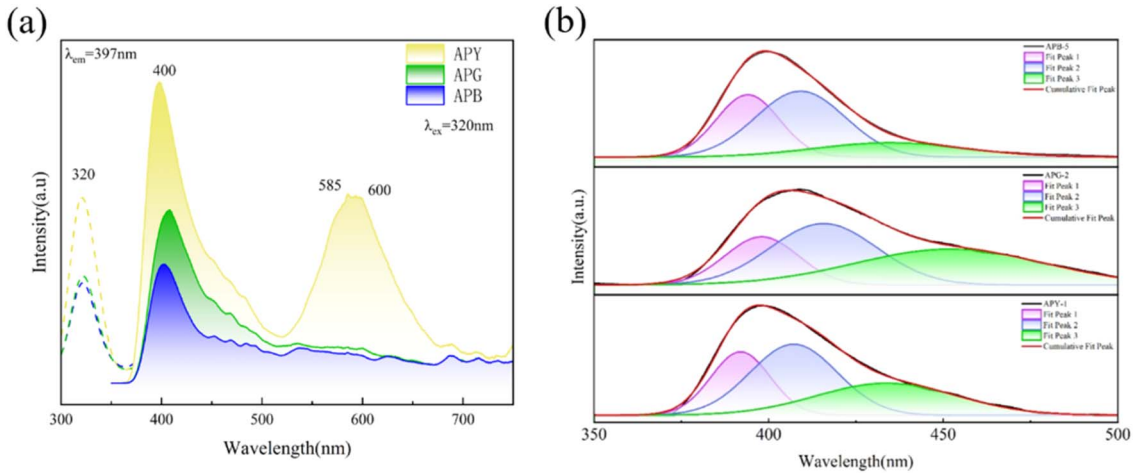

Fig. 8 (a) Fluorescence spectra of three color apatite samples (b) Gaussian fitting of 400 nm emission peaks under 320 nm excitation for some samples of three different color apatite.

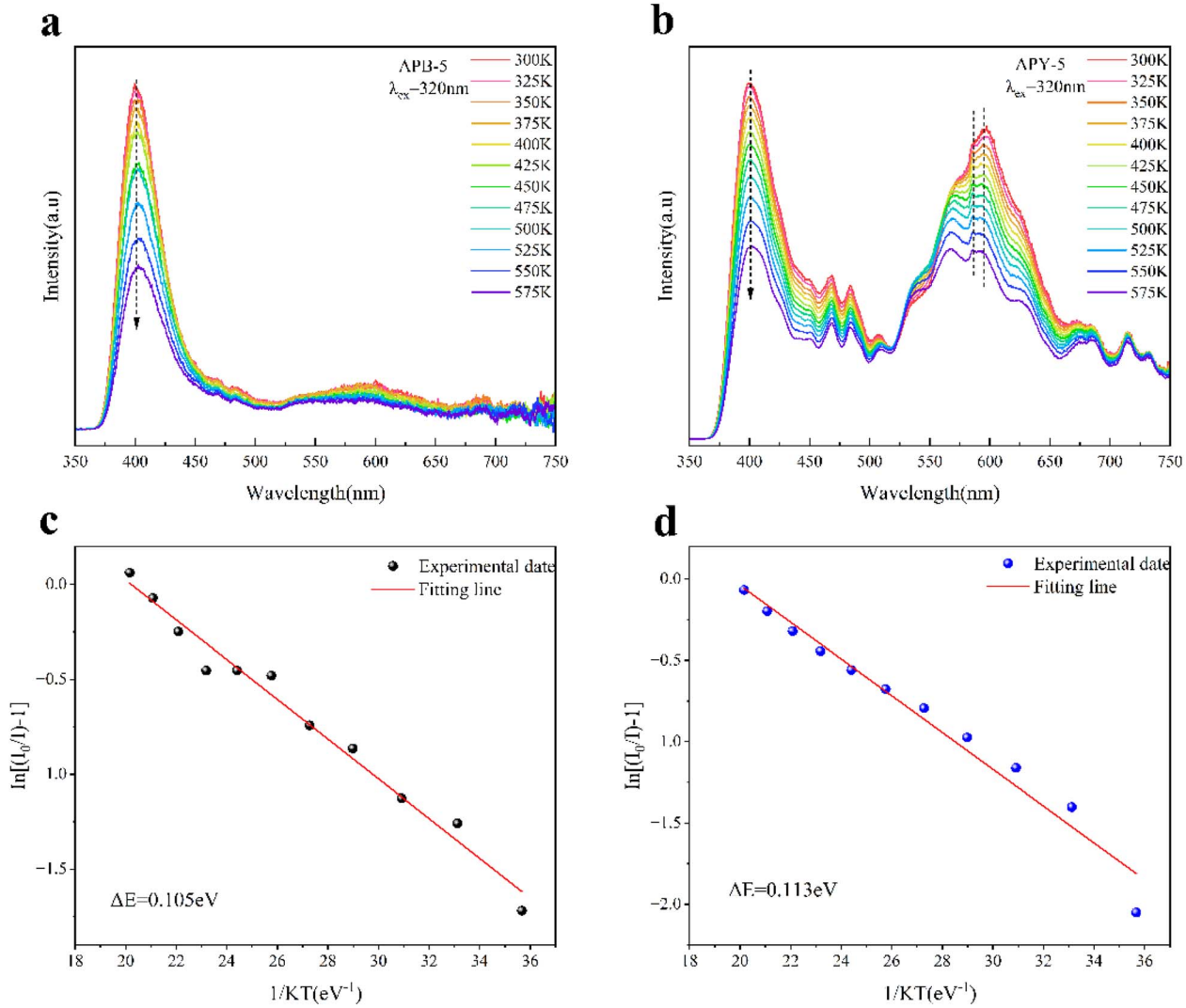

Fig. 9 (a) Variable-temperature emission spectra of APB-5 under 320 nm excitation; (b) variable-temperature emission spectra of APY-5 under 320 nm excitation; (c) plot of $\ln[(I_0/I) - 1]$ *vs.* $1/(kT)$ in the APB-5 sample; (d) plot of $\ln[(I_0/I) - 1]$ *vs.* $1/(kT)$ in the APY-5 sample.

proximity, the Sm ions emit fluorescence when externally excited, while the Pr ions can receive this emission energy and become excited, enhancing the fluorescence emission of the Pr ions. This is due to the suitable coordination environment and energy matching of rare earth ions Sm and Pr at the same lattice position. When the Sm ion is in a higher excited state, the sensitization effect causes the Pr ion to also be in a higher excited state.[34] The effect can be observed through changes in the fluorescence spectrum, in which the emission peak intensity of Pr ions increases and the fluorescence intensity correspondingly enhances. Thus the intensity of the emission peak at 600 nm is also stronger for both the yellow apatite sample than for the green and blue apatite samples.

3.4.2. Variable temperature fluorescence properties. Under different temperature conditions, the spectral properties of APB-5 and APY-5, the most luminescent of the apatite samples, were investigated. Fig. 9a and b show the spectral data of the two samples at different temperatures. The emission peaks are located at 400 nm, 585 nm, and 600 nm. From previous studies, it is known that the emission peak at 400 nm consists of two luminescent centers (Ce and Eu), the emission peak at 585 nm is formed by Sm^{3+}, and the emission peak at 600 nm is formed by Pr^{3+}. The analysis shows that the positions of all diffraction peaks remain essentially constant with increasing temperature, while the emission peaks show a monotonically decreasing trend. The ratio of the emission intensity at 150 °C to the emission intensity at room temperature is commonly used as a measure of good thermal stability.[40] At 425 K, the emission intensity was 81% of the emission intensity at room temperature for the APB-5 and 82% of the emission intensity at room temperature for the APY-5. In order to explain the relationship between the luminescence intensity and temperature, the activation energy E was calculated using Arrhenius formula, where the activation energy is an important parameter of the thermal burst effect and can be expressed by the equation:[36]

$$I(T) = \frac{I_0}{1 + A\exp - \left(\frac{E_b}{K_B T}\right)}$$

where I_0 is the initial emission intensity (300 K), I represents the emission intensity at temperature T (Kelvin temperature), T is the temperature (Kelvin temperature), A is the rate constant, E_b is the temperature quenching activation energy, and K is the Boltzmann constant (8.617×10^{-5} eV K^{-1}). Fig. 9c and d show plots of $\ln[(I_0/I) - 1]$ *versus* $1/(kT)$ in APB-5 and APY-5 samples. As shown, the activation energy of thermal quenching is 0.105 eV for APB-5 and 0.113 eV for APY-5. The larger the value of E_b, the smaller the chance of non-radiative jump and the better the thermal stability, thus indicating that the thermal stability of APY-5 is better than that of APB-5.

4 Conclusions

Apatite samples of three different colors were investigated for structure, composition, spectral characteristics, and fluorescence properties. The XRD results show that the samples are well crystallized and are all fluorapatite. LA-ICP-MS analysis revealed that all three colors of apatite exhibited a "rightward shift" in the distribution of rare earth elements and displayed a negative Ce anomaly, though not significantly so. Among them, the blue and green apatite had a higher negative Eu anomaly index than the yellow apatite sample. The infrared and Raman spectra are essentially the same for all three colors, and the blue and green apatite partial samples show a homogeneous substitution of $[CO_3]^{2-}$ for $[PO_4]^{3-}$. The UV spectra show that the color of yellow apatite comes from the absorption in the red and yellow–green regions, green apatite with some yellow tones comes from the blue–violet region, the yellow–green region and the weak absorption in the orange–red region, and the coloration is mainly related to Nd^{3+}; blue apatite with some green tones comes from the blue-violet region and the strong absorption in the orange-red region, and the coloration is related to MnO_3^- and SO_3^-.Tests comparing the luminescence properties of the three colors of apatite revealed that yellow, blue, and green apatite all produce a strong violet emission band at 400 nm attributed to the $(5d)^5D_{3/2} \rightarrow {}^2F_{7/2}(4f)$ and $(5d)^5D_{3/2} \rightarrow {}^2F_{5/2}(4f)$ transition of Ce^{3+} and the $E_g \rightarrow {}^8S_{7/2}$ transition of Eu^{2+}. Yellow apatite also shows emission bands at 585 nm and 600 nm. These bands are attributed to the ${}^4G_{5/2} \rightarrow {}^5H_{7/2}$ and ${}^1D_2 \rightarrow {}^3H_4$ transition of Sm^{3+} and Pr^{3+}, respectively. It can be seen that the thermal stability of yellow apatite is stronger than that of blue apatite by comparing the relationship between temperature and luminescence intensity of yellow apatite samples and blue apatite samples, and by calculating the activation energies of the two samples. These conclusions help to deepen the understanding of the chromogenic mechanism of apatite and further penetrate into the fluorescence study, indicating that natural apatite is a material matrix with potential research value, promoting the scientific development and progress in related fields.

Author contributions

Wenkai Liang: data collection, analysis, writing the original draft; Nai Wang: review and editing, supervision; Yingrui Gan: investigation; all authors have read and approved the final manuscript.

Conflicts of interest

The authors declare that they have no known competing financial interests or personal relationships that could have appeared to influence the work reported in this paper.

Data availability

All relevant data supporting the finding of this study are available within the manuscript and SI.

Supplementary information include S-1 and S-2. S-1 is LA-ICP-MS results for three colors of apatite. S-2 is globular meteorite fossil standardization results for three colors of apatite. See DOI: https://doi.org/10.1039/d5ra03299g.

Acknowledgements

We would like to thank the laboratory of the School of Gemmology, China University of Geosciences, Beijing, for their help with this experiment.

References

1 J. M. Hughes, M. Cameron and K. D. Crowley, *Am. Mineral.*, 1990, **75**, 295–304.
2 W. P. Nash, *Geochim. Cosmochim. Acta*, 1972, **36**, 1313–1319.
3 B. W. D. Yardley, *Mineral. Mag.*, 1985, **49**, 77–79.
4 H. Mishima, Y. Miake, Y. Matsumoto and T. Hayakawa, *J. Oral Tissue Eng.*, 2018, **16**, 65–73.
5 J. Li, Z. Ma, Y. Yang, J. Huang, R. Zhang and J. Han, *Geol. China*, 2024, 1–30.
6 K. Xing and Q. Shu, *Miner. Deposits*, 2021, **40**, 189–205.
7 H. Liu, L. Liao, X. Pan, K. Su, P. Shuai, Z. Yan, Q. Guo and L. Mei, *Open Ceram.*, 2022, **10**, 100251.
8 Q. Guo, B. Ma, L. Liao, M. Molokeev, L. Mei and H. Liu, *Ceram. Int.*, 2016, **42**, 11687–11691.
9 K. Li, D. Geng, M. Shang, Y. Zhang, H. Lian and J. Lin, *J. Phys. Chem.*, 2014, **118**, 11026–11034.
10 N. An, F. Xu, Q. Guo, L. Liao, L. Mei and H. Liu, *RSC Adv.*, 2020, **10**, 11608–11614.
11 H. Liu, L. Liao and Z. Xia, *RSC Adv.*, 2014, **4**, 7288–7295.
12 J. Zhang, Q. Guo, L. Liao, Y. Wang, M. He, H. Ye, L. Mei, H. Liu, T. Zhou and B. Ma, *RSC Adv.*, 2018, **8**, 38883–38890.
13 R. Reisfeld, M. Gaft, G. Boulon, C. Panczer and C. K. Jrgensen, *J. Lumin.*, 1996, **69**, 343–353.
14 E. Cantelar, G. Lifante, T. Calderón, R. Meléndrez, A. Millán, M. Alvarez and M. Barboza-Flores, *J. Alloys Compd.*, 2001, **323**, 851–854.
15 M. Gaft, R. Reisfeld, G. Panczer, S. Shoval, B. Champagnon and G. Boulon, *J. Lumin.*, 1997, **72**, 572–574.
16 M. Gaft, R. Reisfeld, G. Panczer, E. Uspensky, B. Varrel and G. Boulon, *Opt. Mater.*, 1999, **13**, 71–79.
17 S. Bodył, *Mineralogia*, 2010, **40**, 85–94.
18 M. Czaja, S. Bodył, P. Głuchowski, Z. Mazurak and W. Strek, *J. Alloys Compd.*, 2008, **451**, 290–292.
19 S. Zhang, *Spectroscopy of Rare Earth Ions Spectral Properties and Spectral Theory*, 2008.
20 M. Vignoles, G. Bonel, D. Holcomb and R. Young, *Calcif. Tissue Int.*, 1988, **43**, 33–40.
21 B. Gnter and T. Georg, *Contr. Mineral. Petrol.*, 1989, **101**, 394–401.
22 F. C. M. Driessens, R. M. H. Verbeeck and H. J. M. Heijligers, *Inorg. Chim. Acta*, 1983, **80**, 19–23.
23 H. B. Ribeiro, K. J. Guedes, M. V. B. Pinheiro, S. Greulich-Weber and K. Krambrock, *Phys. Status Solidi C*, 2005, **2**, 720–723.
24 A. J. Miles, C. M. Graham, C. J. Hawkesworth, M. R. Gillespie, R. W. Hinton and G. D. Bromiley, *Geochim. Cosmochim. Acta*, 2014, **132**, 101–119.
25 L. Han, X. Huang, J. Li, P. He and J. Yao, *Acta Petrol. Sin.*, 2016, **32**, 746–758.
26 J. Gillespie, C. L. Kirkland, P. D. Kinny, A. Simpson, S. Glorie and K. Rankenburg, *Geochim. Cosmochim. Acta*, 2022, **338**, 121–135.
27 M. J. Streck and J. H. Dilles, *Geology*, 1998, **26**, 523–526.
28 M. R. Carroll and M. J. Rutherford, *J. Petrol.*, 1987, **28**, 781–801.
29 C. H. Yoder, M. M. Bollmeyer, K. R. Stepien and R. N. Dudrick, *J. Earth Planet. Sci. Lett.*, 2019, **104**, 869–877.
30 P. Chindudsadeegul and M. Jamkratoke, *Spectrochim. Acta A Mol. Biomol. Spectrosc.*, 2018, **204**, 276–280.
31 L. G. Gilinskaya and K. I. Mashkovets, *J. Struct. Chem.*, 1995, **36**, 76–86.
32 R. Wu, F. Zhu and F. Bai, *Geol. Rev.*, 2001, 255–280.
33 Y. Gu, J. Pei, Y. Zhang, x. Yin, M. Yu and X. Lai, *Spectrosc. Spectral Anal.*, 2024, **44**, 181–187.
34 M. Gaft and G. Panczer, *Phys. Chem. Miner.*, 2001, **28**, 347–363.
35 A. D. Sontakke, J. Ueda and S. Tanabe, *J. Non-Cryst. Solids*, 2016, **431**, 150–153.
36 Y. Sun, H. Guo, F. Jiang, R. Yuan, J. Zhang, X. Zhang, T. Zhou, Y. Qiu, b. Zhang and K. Xu, *Appl. Surf. Sci.*, 2013, **283**, 258–262.
37 C. K. Jorgensen, *Modern Aspects of Ligand Field Theory*, 1971.
38 M. Czaja, S. Bodył, R. Lisiecki and Z. Mazurak, *Phys. Chem. Miner.*, 2010, **37**, 425–433.
39 H. Zhou, Q. Wang, M. Jiang, X. Jiang and Y. Jin, *Int. J. Inorg. Chem.*, 2015, **44**, 13962–13968.
40 K. Biswas, A. D. Sontakke and K. Annapurna, *Int. J. Appl. Glass Sci.*, 2012, **3**, 154–162.